

Measurement of molybdenum ion density for L-mode and H-mode plasma discharges in the EAST tokamak

Yongcai Shen(沈永才), Hongming Zhang(张洪明), Bo Lyu(吕波), Yingying Li(李颖颖), Jia Fu(符佳), Fudi Wang(王福地), Qing Zang(臧庆), Baonian Wan(万宝年), Pan Pan(潘盼), Minyou Ye(叶民友)

Citation: Chin. Phys. B . 2020, 29(6): 065206 . **doi:** 10.1088/1674-1056/ab8456
Journal homepage: http://cpb.iphy.ac.cn; http://iopscience.iop.org/cpb

What follows is a list of articles you may be interested in

Plasma shape optimization for EAST tokamak using orthogonal method

Yuan-Yang Chen(陈远洋), Xiao-Hua Bao(鲍晓华), Peng Fu(傅鹏), Ge Gao(高格)

Chin. Phys. B . 2019, 28(1): 015201 . **doi:** 10.1088/1674-1056/28/1/015201

Radiative divertor behavior and physics in Ar seeded plasma on EAST

Jingbo Chen(陈竞博), Yanmin Duan(段艳敏), Zhongshi Yang(杨钟时), Liang Wang(王亮), Kai Wu(吴凯), Kedong Li(李克栋), Fang Ding(丁芳), Hongmin Mao(毛红敏), Jichan Xu(许吉禅), Wei Gao(高伟), Ling Zhang(张凌), Jinhua Wu(吴金华), Guang-Nan Luo(罗广南), EAST Team

Chin. Phys. B . 2017, 26(9): 095205 . **doi:** 10.1088/1674-1056/26/9/095205

A divertor plasma configuration design method for tokamaks

Yong Guo(郭勇), Bing-Jia Xiao(肖炳甲), Lei Liu(刘磊), Fei Yang(杨飞), Yuehang Wang(汪悦航), Qinglai Qiu(仇庆来)

Chin. Phys. B . 2016, 25(11): 115201 . **doi:** 10.1088/1674-1056/25/11/115201

Optimized calculation of the synergy conditions between electron cyclotron current drive and lower hybrid current drive on EAST

Wei Wei(韦维), Bo-Jiang Ding(丁伯江), Y Peysson, J Decker, Miao-Hui Li(李妙辉),Xin-Jun Zhang(张新军), Xiao-Jie Wang(王晓洁), Lei Zhang(张磊)

Chin. Phys. B . 2016, 25(1): 015201 . **doi:** 10.1088/1674-1056/25/1/015201

Characterization of plasma current quench during disruption in EAST tokamak

Chen Da-Long, Granetz Robert, Shen Biao, Yang Fei, Qian Jin-Ping, Xiao Bing-Jia

Chin. Phys. B . 2015, 24(2): 025205 . **doi:** 10.1088/1674-1056/24/2/025205

Measurement of molybdenum ion density for L-mode and H-mode plasma discharges in the EAST tokamak*

Yongcai Shen(沈永才)[1,2], Hongming Zhang(张洪明)[1], Bo Lyu(吕波)[1,†], Yingying Li(李颖颖)[1], Jia Fu(符佳)[1], Fudi Wang(王福地)[1], Qing Zang(臧庆)[1], Baonian Wan(万宝年)[1], Pan Pan(潘盼)[2], Minyou Ye(叶民友)[3], and the EAST team

[1] *Institute of Plasma Physics, Chinese Academy of Sciences, Hefei* 230031, *China*
[2] *School of Mathematics and Physics, Anqing Normal University, Anqing* 246011, *China*
[3] *Department of Engineering and Applied Physics, University of Science and Technology of China, Hefei* 230026, *China*

(Received 6 January 2020; revised manuscript received 29 February 2020; accepted manuscript online 30 March 2020)

We report the measurement of total molybdenum ion density for L-mode and H-mode plasmas on EAST using spectral lines observation and calculation based on an impurity transport code. A flat-filed extreme ultraviolet spectrometer with some spatial resolution is used to obtain the radial profiles of molybdenum spectral line emissions. The absolute calibration for the extreme ultraviolet spectrometer is finished by comparing the calculated bremsstrahlung intensity with the readings of CCD detector. Molybdenum ion transport study is performed using the radial ion density profiles and one-dimensional impurity transport code STRAHL. The total molybdenum density profiles are determined from the transport analysis. The molybdenum density during L-mode and H-mode phases are obtained, which are about 3 and 4 orders of magnitude smaller than the electron density, respectively. An inward pinch is found during the H-mode phase that leads to the peaked profile of molybdenum density.

Keywords: EAST, EUV spectroscopy, molybdenum density, L-mode and H-mode

PACS: 52.70.Kz, 52.25.Vy, 32.30.Rj **DOI:** 10.1088/1674-1056/ab8456

1. Introduction

Research of the impurity behavior is important for tokamak plasma operations since the degradation of plasma performance can be avoided by controlling the impurity content in the core and the impurity radiation loss at the edge.[1] It has been observed that impurity profiles tend to be more peaked than the main ion profile in many experiments, which is known as the impurity accumulation.[2] Impurity accumulation is found to be more severe for heavier impurity species.[3] On the EAST tokamak, heavy impurity species are mainly from metal impurities such as iron, copper, molybdenum, and tungsten,[4] and impurity accumulation is often observed, especially during the high-density H-mode plasma operations.

Spectroscopy is a unique method to measure the impurity spectra and to study the impurity behavior. In particular, extreme ultraviolet (EUV) spectroscopy is an excellent tool for the impurity diagnostics in high-temperature plasmas of fusion devices.[5–10] A flat-filed grating spectrometer that utilizes varied line spacing gratings to image the spectrum of 5–50 nm was installed in the EAST tokamak to monitor core impurity emission profile for impurity transport investigations.[11] Absolute intensity calibration of the spectrometers was performed by using the bremsstrahlung continuum in ohmic discharges on EAST tokamak.[12] Experimental impurity transport investigations have been performed in many magnetic confinement devices and most of the impurity transport studies have been carried out using the spatial profiles of absolute intensities of spectral emissions from spectroscopic measurement and comparison with an impurity transport code to determine the transport coefficients.[13–18] A future reactor will use high-Z plasma facing components (PFCs) such as tungsten in order to provide low erosion, sputtering yield and tritium retention. Since 2012, the first wall material of EAST has been mostly changed into molybdenum, which makes molybdenum as the most commonly seen metal impurity. Molybdenum density measurement can be useful for the molybdenum behavior study and evaluation of its effect on plasma performance. Among the metallic impurities that can be used for transport study, molybdenum has a good and well assessed knowledge base of the atomic physics.

In the rest of this paper, the experimental setup and the observations of molybdenum spectral lines are presented first. Then the absolute value calibration for the EUV spectrometer is illustrated in Section 3. Next, the measurement of molybde-

*Project supported by the National Key Research and Development Program of China (Grant No. 2017YFE031300), the Key Program of Research and Development of Hefei Science Center of China (Grant No. 2017HSC-KPRD002), the National Natural Science Foundation of China (Grant No. 11805231), the Natural Science Foundation of Anhui Province of China (Grant Nos. 1908085J01, 1808085QA14, and 1908085QF274), the ASIPP Science and Research Fund of China (Grant No. DSJJ-17-03), Collaborative Innovation Program of Hefei Science Center, CAS (Grant No. 2019HSC-CIP005), and Anqing Normal University Research Project, China (Grant Nos. 043-180079 and 044-140001000024).

†Corresponding author. E-mail: blu@ipp.ac.cn

© 2020 Chinese Physical Society and IOP Publishing Ltd

num density during L-mode and H-mode phases are studied in Section 4 and the last part is the conclusion.

2. Experimental setup and the observations of molybdenum lines

The experimental advanced superconducting tokamak (EAST) is the first fully superconducting tokamak dedicated to high-performance and long-pulse operation, with elongated divertor configuration (an elongation ratio $\kappa < 1.9$).[19] The tokamak has a major radius of $R \sim 1.85$ m and a minor radius of $a = 0.4$–0.45 m. Now, the EAST is equipped with lower hybrid current drive (LHCD), ion cyclotron range of frequency (ICRF), neutral beam injection (NBI), and electron cyclotron resonance heating (ECRH) systems, as the main auxiliary heating and current drive systems. Upper divertors are mainly made up of tungsten and the first wall is composed of molybdenum, which constitute the main part of plasma facing materials (PFMs) on the EAST. The spatial profiles of molybdenum spectral lines are monitored using an EUV spectrometer, which consists of two main parts: an adjustable entrance slit with a width of 0–0.5 mm determining the spectral resolution and height at 0–1 mm controlling the space resolution, a varied-line-spacing (VLS) spherically concaved holographic grating, and a back-illuminated charge coupled device (CCD) detector. The EUV spectrometer is now installed at the EAST's port C and is attached to the end of vacuum pumping duct. The optical layout of the spectrometer can be seen in Fig. 1(a). The current setup is able to cover 0–450 mm above the equatorial plane. The spatial profile measurement of the impurity for the spectrometer is illustrated in Fig. 1(b) from the pinhole imaging setup.

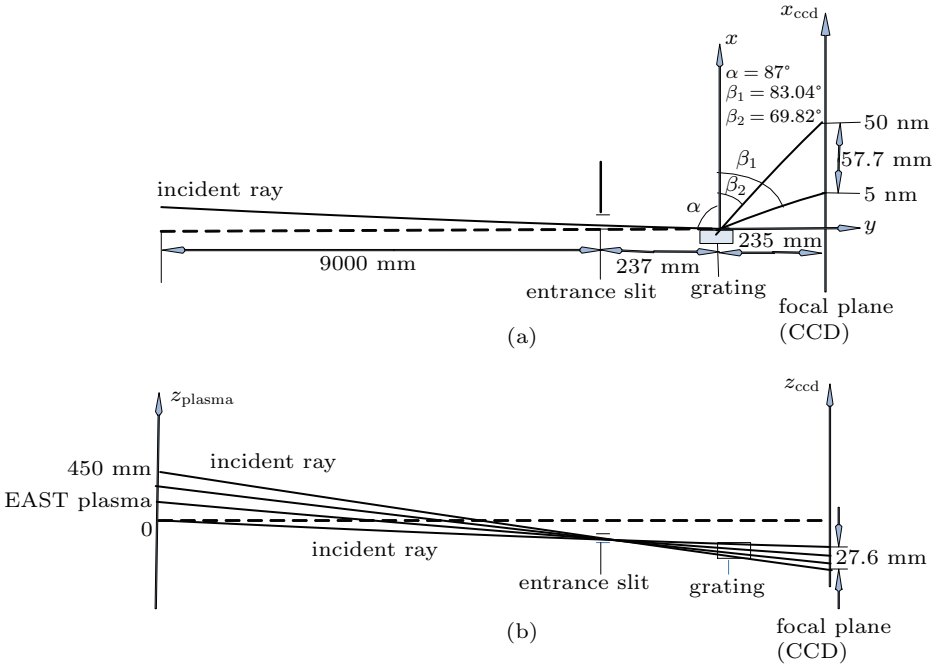


Fig. 1. Schematic drawing of space-resolved spectrometer (a) optical path in top view and (b) principle of spatial resolution in vertical view.

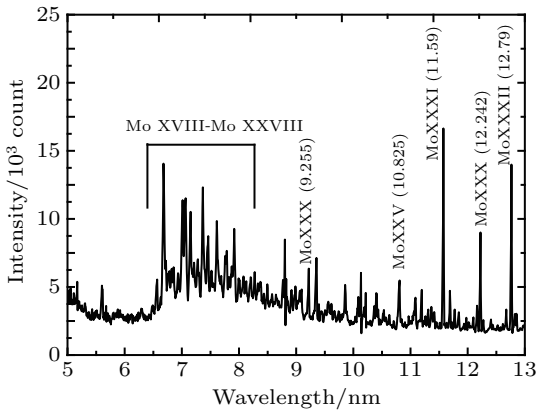


Fig. 2. Mo spectrum in 5–13 nm.

Figure 2 presents a typical EUV spectrum from highly ionized molybdenum in the wavelength of 5–13 nm. A complicated structure is seen between 6.5 nm and 8.5 nm, mostly consisting of ion charge states of Mo XXIV–Mo XXVII. Isolated Mo XXX–XXXII line emissions observed in 10–13 nm are not difficult to identify when the central electron temperature is high enough considering their high ionization energy (Mo XXX: 1601 eV, Mo XXXI: 1726 eV, Mo XXXII: 1791 eV), so Mo XXX at 12.242 nm, Mo XXXI at 11.5988 nm and Mo XXXII at 12.7868 nm are chosen to carry out molybdenum density calculation.

3. Absolute intensity calibration of EUV spectrometer

Absolute intensity calibration for the EUV spectrometer is technically difficult due to the lack of appropriate standard light source in the EUV range. In this paper, the absolute intensity calibration is conducted by comparing the calculated bremsstrahlung intensity with the measured bremsstrahlung intensity in the EUV range.

The continuum radiation can be divided into bremsstrahlung and recombination radiation. In the present fusion plasma with high electron temperature, the contribution of recombination radiation is very small compared with bremsstrahlung. Therefore, in our case we only consider continuum radiation as the bremsstrahlung. The bremsstrahlung power can be expressed as[20]

$$U_{\rm brem} = 1.9\times10^{-28}\frac{n_{\rm e}^2 Z_{\rm eff}^2 g_{\rm ff}}{\lambda^2 T_{\rm e}^{1/2}} \times \exp\left(\frac{-12395}{\lambda T_{\rm e}}\right)\ [\mathrm{W\cdot cm^{-3}\cdot \AA^{-1}}], \quad (1)$$

where $n_{\rm e}$ is the electron temperature in units of cm^{-3}, $T_{\rm e}$ is the electron temperature in units of eV, $Z_{\rm eff}$ is the effective ion charge, $g_{\rm ff}$ is the free-free Gaunt factor, and λ is the corresponding wavelength in units of Å. The bremsstrahlung power along the line of light can be calculated when taking into account the plasma parameters. Electron temperature and density is measured by Thomson scattering diagnostics.[21]

Since the measured intensity of bremsstrahlung is presented by the counting rate of photons, equation (1) can be changed into

$$N_{\rm brem} = \frac{U_{\rm brem}}{h\nu}, \quad (2)$$

where $h\nu$ is the photon energy.

Finally, the absolute intensity calibration of EUV spectrometer can be obtained by comparing the observed EUV bremsstrahlung radiation profile with the calculated EUV bremsstrahlung and the absolute intensity calibration factor can be expressed as

$$S = \frac{N_{\rm brem_EUV}}{N_{\rm obser_EUV}}, \quad (3)$$

where $N_{\rm obser_EUV}$ is the observed counts of CCD reading at the same wavelength as $N_{\rm brem_EUV}$.

Ohmic discharges are chosen for calculating the bremsstrahlung intensity. The parameters of the discharge are $I_{\rm p} = 400$ kA, $B_{\rm t} = 2$ T, and $Z_{\rm eff} = 3$. The Gaunt factor is calculated with the code RADZ.[12] From 5.8 nm to 20.1 nm, the chosen wavelength intervals for absolute intensity calibration of the spectrometer are listed in Table 1. $N_{\rm brem}$ can be calculated by Eqs. (1) and (2) using the parameters obtained from other diagnostics. Then the absolute intensity calibration factor of the EUV spectrometer has been calculated by Eq. (3). The results are shown in Table 2 as well as Ref. [22].

Table 1. The chosen bremsstrahlung continuum wavelength intervals for absolute calibration of the EUV spectrometer.

Wavelength range/nm	Central wavelength/nm
5.6–6.0	5.8
6.1–6.5	6.3
7.6–8.0	7.8
8.1–8.3	8.2
8.9–9.3	9.1
9.6–10	9.8
11.2–10.6	10.4
11–11.4	11.2
11.8–12.2	12
12.6–13	12.8
13.5–13.9	13.7
14.3–14.7	14.5
15.1–15.5	15.3
15.9–16.3	16.1
16.7–17.1	16.9
17.5–17.9	17.7
18.3–18.7	18.5
19.1–19.5	19.3
19.9–20.3	20.1

Table 2. Sensitivity calibration coefficients of the present EUV system.

Central wavelength/nm	Absolute calibration coefficient
5.8	2.6533850×10^8
6.3	2.5305166×10^8
7.8	2.5335634×10^8
8.2	2.6703333×10^8
9.1	3.2583642×10^8
9.8	3.6774128×10^8
10.4	3.9531347×10^8
11.2	4.3139325×10^8
12	4.7845677×10^8
12.8	4.9811859×10^8
13.7	5.0487075×10^8
14.5	4.9544579×10^8
15.3	5.1624842×10^8
16.1	5.4101146×10^8
16.9	5.7908230×10^8
17.7	6.3613862×10^8
18.5	6.2681472×10^8
19.3	5.9795315×10^8
20.1	5.4957427×10^8

4. Molybdenum density measurement during L-mode and H-mode phases

The waveform of a typical EAST H-mode discharge together with the time evolution of Mo XXXI intensity at 11.59 nm is shown in Fig. 3. The plasma current is 400 kA. At the beginning it only has ohmic heating and the loop voltage is high. Mo XXXI intensity keeps at a low level. When LHCD is injected at $t = 1.2$ s, the loop voltage begins to decrease. ICRF wave is injected at $t = 2.6$ s and the discharge enters the

H-mode phase suddenly, as can be seen in the abrupt $D\alpha$ signal drop. In the meantime, Mo XXXI signal builds up and then rises quickly. Mo XXXI intensity reaches its highest value at $t = 3.8$ s as a result of impurity accumulation. The profiles of Mo XXX, Mo XXXI and Mo XXXII in L-mode ($t = 2.4$ s) and H-mode ($t = 3.8$ s) phases are shown in Fig. 4. By multiplying the sensitivity calibration coefficients in Table 2, the chord-integrated brightness profiles of three lines can be obtained as shown in Fig. 5.

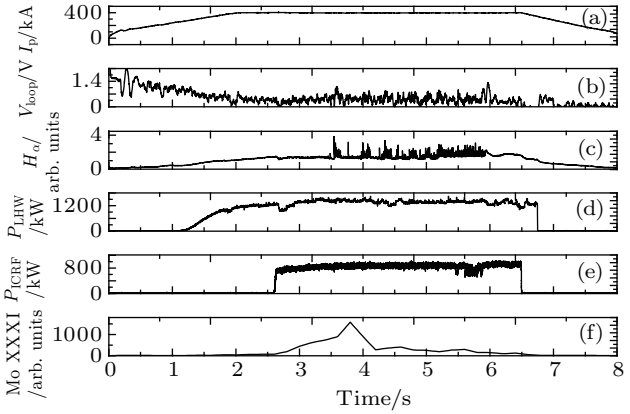


Fig. 3. The time evolution of shot 38300: (a) plasma current, (b) loop voltage, (c) H_α intensity, (d) LHCD power, (e) ICRF power, and (f) intensity of Mo XXXI (11.59 nm).

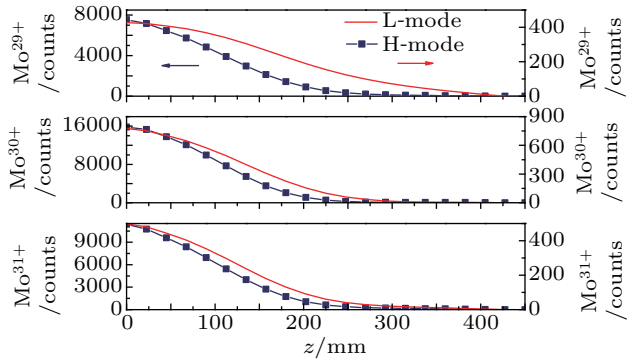


Fig. 4. The intensity profiles of Mo XXX, Mo XXXI and Mo XXXII during L-mode ($t = 2.4$ s) and H-mode ($t = 3.8$ s) phases from shot 38300.

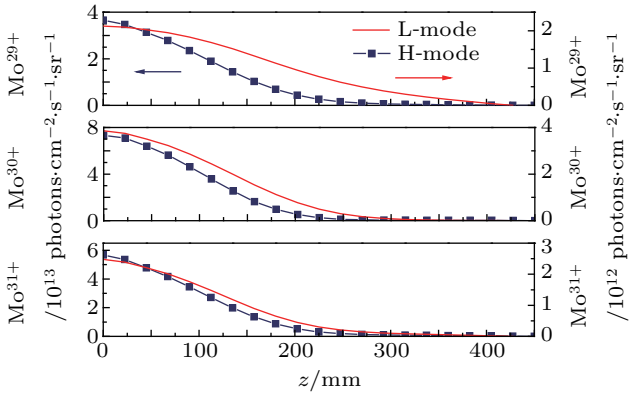


Fig. 5. The chord-integrated brightness profiles of Mo XXX, Mo XXXI and Mo XXXII during L-mode ($t = 2.4$ s) and H-mode ($t = 3.8$ s) phases from shot 38300.

The local radial emissivity profiles can be obtained using an Abel-like matrix inversion technique. The relationship between the line integrated brightness and the local emissivity can be expressed as[23]

$$B_i = \sum L_{ij} E_j, \tag{4}$$

where L_{ij} is the path length of the i-th chord through the j-th zone between two adjacent magnetic surfaces and can be determined solely from geometry, E_j is the j-th zone emissivity and B_i is the i-th chord brightness.

The emissivity E_j can be obtained by inverting Eq. (4) and expressed as

$$E_j = \sum L_{ij}^{-1} B_i. \tag{5}$$

After Abel inversion, the emissivity profiles of Mo XXX, Mo XXXI and Mo XXXII during L- and H-mode phases are plotted in Fig. 6. It can be seen that the three line intensity profiles are centrally peaked.

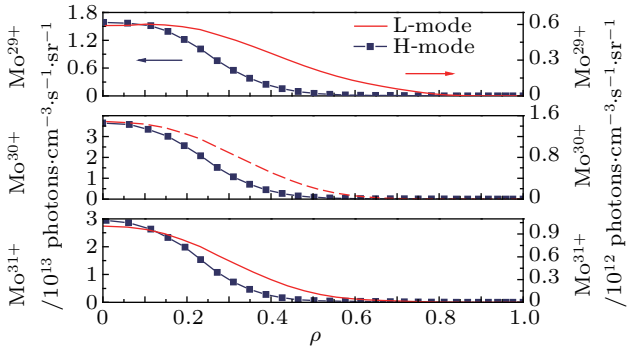


Fig. 6. The emissivity profiles of Mo XXX, Mo XXXI and Mo XXXII as a function of ρ during L-mode ($t = 2.4$ s) and H-mode ($t = 3.8$ s) phases from shot 38300.

The emissivity of a particular transition from the initial state to the final state can be expressed as

$$E_{Z,i,j} = n_Z(\rho) \cdot n_e(\rho) \cdot \mathrm{PEC}_{Z,i,j}(\rho), \tag{6}$$

where i is the initial state, j is the final state; n_Z and n_e are the impurity and electron densities, and PEC is the photon emissivity coefficient depending on both electron density and temperature and can be obtained from the Atomic Data and Analysis Structure (ADAS) database.[24]

The radial profile of Mo^{29+} spectral emission at 12.242 can be calculated by

$$E_{Mo^{29+}}^{12.242\ \mathrm{nm}} = n_Z(\rho) \cdot n_e(\rho) \cdot \mathrm{PEC}^{\mathrm{exc}}(\rho) + n_{Z+1}(\rho) \cdot n_e(\rho) \cdot \mathrm{PEC}^{\mathrm{rec}}(\rho) + n_{Z+1}(\rho) \cdot n_H(\rho) \cdot \mathrm{PEC}^{\mathrm{cx}}(\rho), \tag{7}$$

where $\mathrm{PEC}^{\mathrm{exc}}$, $\mathrm{PEC}^{\mathrm{rec}}$ and $\mathrm{PEC}^{\mathrm{cx}}$ are the PECs for excitation recombination and charge exchange, respectively; n_Z and n_{Z+1} are the impurity density of the ground level of a specific ionization state and next higher ionization state, and n_H is the neutral hydrogen density. As there is no neutral beam injection for the discharges analyzed here, the contribution of charge exchange can be neglected. Considering that the plasma is at

the steady-state phase, the recombination term can also be neglected. The remaining important term is from excitation and the radial profile of PEC for excitation can be calculated from the ADAS database by inserting the radial profiles of electron density and temperature. Then the density profile of Mo XXX can now be expressed as

$$n_{\mathrm{Mo}^{29+}}(\rho) = E^{12.242\ \mathrm{nm}}_{\mathrm{Mo}^{29+}} / [n_{\mathrm{e}}(\rho) \cdot \mathrm{PEC}^{\mathrm{exc}}_{\lambda=12.242\ \mathrm{nm}}(\rho)]. \quad (8)$$

For Mo XXXI at 11.5988 nm and Mo XXXII at 12.7868 nm, the density profile can also be calculated in the same way as Mo XXX. The electron density and temperature are measured by Thomson scattering diagnostic and the profiles are shown in Fig. 7. By using their profiles, the radial profiles of PEC for excitation can be obtained and the density profiles can be calculated using Eq. (8).

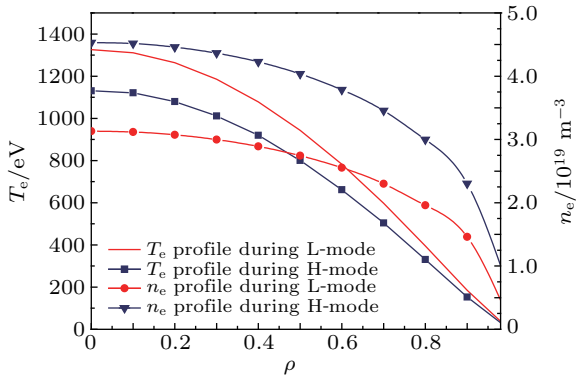


Fig. 7. The electron density and and temperature profiles measured by Thomson scattering.

In order to calculate the total molybdenum density, the molybdenum density's radial profile has been computed using a 1D impurity code, STRAHL, and matched with the measured results.[25] The STRAHL code solves the coupled radial impurity transport equations for ions at all possible ionization stages. For one charge stage Z, the coupled radial impurity transport equation can be expressed as

$$\frac{\partial n_Z}{\partial t} = \frac{1}{r}\frac{\partial}{\partial r}\left(D\frac{\partial n_Z}{\partial r} - v n_Z\right) + Q_Z, \quad (9)$$

where D is the diffusion coefficient and v is the convection velocity. Both of them are assumed to be time-independent and to be the same for all the ionization stages of impurity ions. The source/sink term Q couples the transport equation of each ionization stage to the neighboring charge stages as follows:

$$\begin{aligned} Q_Z = & -(n_{\mathrm{e}}S_Z + n_{\mathrm{e}}\alpha_Z + n_{\mathrm{H}}C_Z)n_Z + n_{\mathrm{e}}S_{Z-1}n_{Z-1} \\ & + (n_{\mathrm{e}}\alpha_{Z+1} + n_{\mathrm{H}}C_{Z+1})n_{Z+1}, \end{aligned} \quad (10)$$

where S is the rate coefficient for ionization, α is the rate coefficient for recombination (radiative and dielectronic), and C is for charge exchange recombination.[24,26] The main inputs to the STRAHL code are electron density and temperature profiles, impurity source rate, diffusion, convective and atomic physics data from ADAS for ionization and recombination calculations. Impurity ion densities of Mo^{29+}, Mo^{30+}, and Mo^{31+} are calculated by the STRAHL code from the molybdenum ionization balance together with the given plasma parameters.

Running of the STRAHL code starts with initial guesses of diffusion and convective coefficients to compute the impurity radial profiles. Subsequently, diffusion and convective coefficients iterate and converge until the best fit of simulated ion density profiles to the measured ones are obtained. The final D and v are plotted in Figs. 8 and 9. Figure 10 shows the best-fit calculated ion density profiles of Mo XXX, Mo XXXI and Mo XXXII during both L-mode and H-mode phases. Compared with impurity diffusion coefficient during the L-mode phase, it is smaller during the H-mode phase. The convective velocity is positive and shows an increasing trend from the core to the edge area during L-mode phase while it is negative within $\rho < 0.6$, which means that the convection velocity v in the core plasma reverses from outward ($v > 0$) to inward ($v > 0$) after L- to H-mode transition. These facts indicate that molybdenum impurities undergo inward transport during the H-mode phase, which can lead to impurity accumulation in the core region. Molybdenum ion density of all ionization stages can be obtained after the running the STRAHL code and the total molybdenum density can be calculated by adding these ion density. The molybdenum densities during L-mode and H-mode phases are shown in Fig. 11, which are of about 3–4 orders of magnitude smaller than the electron density. The peaked profile of molybdenum density during H-mode phase can be a result of inward transport.

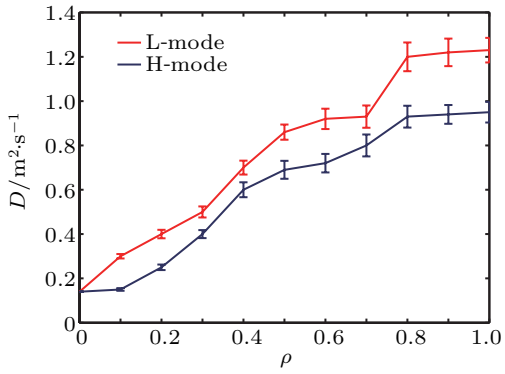


Fig. 8. Radial profiles of diffusion coefficients during L-mode and H-mode phases.

Impurity radiation power density can be estimated according to $P_Z = n_{\mathrm{e}} n_Z L_Z$, where L_Z represents the line cooling rate.[27] In our case, central electron temperature is around 1.3 keV and 1.1 keV, and the central electron density are 3×10^{19} m^{-3} and 4.5×10^{19} m^{-3} during L-mode and H-mode, respectively. If we consider a molybdenum cooling factor of $L_{\mathrm{Mo}} \approx 7 \times 10^{-32}$ W $\cdot$ m^3, the radiated power density of molybdenum in the core region can be around 140 kW/m^3 and 20 kW/m^3 during H-mode and L-mode phases.[27]

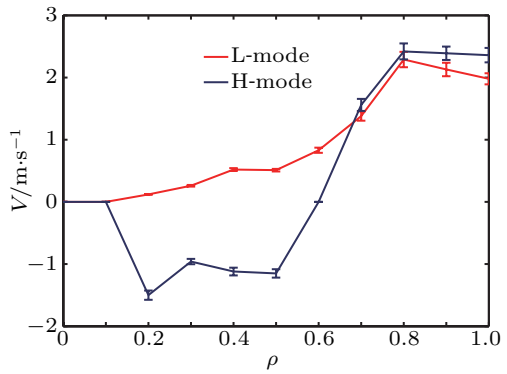


Fig. 9. Radial profiles of convective velocities during L-mode and H-mode phases.

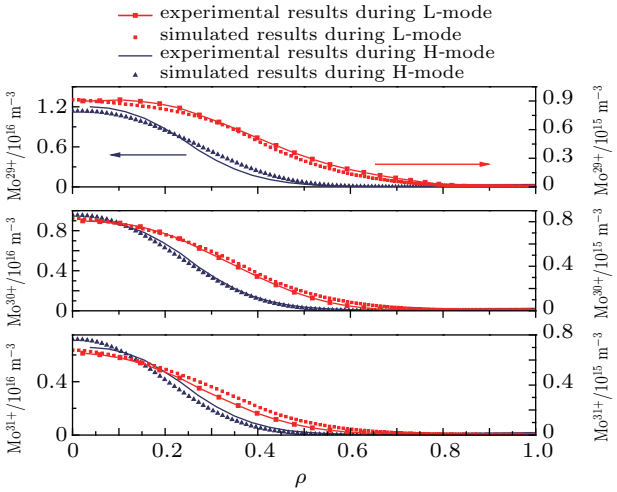


Fig. 10. The best-fit calculated ion density profiles of Mo^{29+}, Mo^{30+} and Mo^{31+} during L-mode and H-mode phases associated with the experimental results.

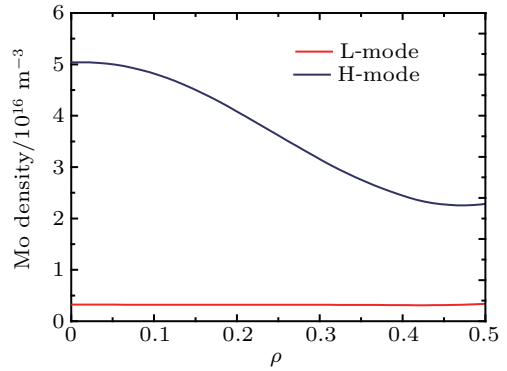


Fig. 11. Total molybdenum density obtained during L-mode and H-mode phases from the simulation results.

5. Conclusion

The extreme ultraviolet spectrometer previously used on the EAST tokamak has been calibrated by comparing the calculated bremsstrahlung radiation intensity with the reading of CCD's detector. The reconstructed emission profiles are obtained at the core plasma for Mo XXX, Mo XXXI and Mo XXXII. To facilitate next-step impurity transport studies, total molybdenum density profiles during L-mode and H-mode phases are obtained using the spectral lines and the STRAHL code. The results show that the molybdenum density is 3–4 orders of magnitude smaller than electron densities in typical EAST plasmas. Impurity accumulation happens during H-mode phase as a result of inward pinch in core plasma. Estimates of molybdenum radiated power density are 140 kW/m^3 and 20 kW/m^3 in core plasma during H-mode and L-mode phases. The present EUV spectrometer is designed to study the impurity behavior and impurity transport. By using the present method, the impurity accumulation behavior and the related transport mechanism will be studied in the future, which will be useful for exploring methods for relieving impurity accumulation.

Acknowledgments

The authors are grateful to the diagnostic group, and the operation team of the EAST tokamak.

References

[1] Cui Z Y, Morita S, Zhou H Y *et al.* 2013 *Nucl. Fusion* **53** 093001
[2] Dux R, Giroud C, Neu R *et al.* 2003 *J. Nucl. Mater.* **313-316** 1150
[3] Dux R and Peeters A G 2000 *Nucl. Fusion* **40** 1721
[4] Shen Y C, Lyu B, Du X W *et al.* 2015 *Plasma. Sci. Technol.* **17** 183
[5] Dong C F, Morita S, Goto M and Wang E H 2011 *Rev. Sci. Instrum.* **82** 113102
[6] Lepson J K, Beiersdorfer P, Clementson J *et al.* 2010 *J. Phys. B: At. Mol. Opt. Phys.* **43** 144018
[7] Cui Z Y, Morita S, Fu B Z *et al.* 2010 *Rev. Sci. Instrum.* **81** 043503
[8] Beiersdorfer P, Brown G V, Kamp J B *et al.* 2011 *Can. J. Phys.* **89** 653
[9] Shen Y, Du X, Zhang W, Wang Q *et al.* 2013 *Nucl. Instrum. Methods Phys. Res. Sect. A* **700** 86
[10] Shen Y C, Lu B, Du X W *et al.* 2013 *Fusion Eng.* **88** 3072
[11] Shen Y C, Lyu B, Wang F D *et al.* 2016 *Chin. Phys. Lett.* **33** 065205
[12] Zhang H M, Shen Y C, Fu J *et al.* 2013 *Nucl. Fusion. Plasma Phys.* **33** 312 (in Chinese)
[13] Dong C F, Wang E H, Morita S, Goto M *et al.* 2013 *Plasma Sci. Technol.* **15** 230
[14] Kuldkepp M, Brunsell P R, Cecconello M *et al.* 2006 *Phys. Plasmas* **13** 092506
[15] Leigheb M, Romanelli M, Gabellieri L *et al.* 2007 *Plasma Phys. Control. Fusion.* **49** 1897
[16] Puiatti M E, Valisa M, Angioni C *et al.* 2006 *Phys. Plasmas* **13** 042501
[17] Delgado-Aparicio L, Stutman D, Tritz K *et al.* 2011 *Nucl. Fusion* **51** 083047
[18] Chowdhuri M B, Ghosh J, Banerjee S *et al.* 2015 *Nucl. Fusion* **55** 023006
[19] Wan B N, Liang Y F, Gong X Z *et al.* 2017 *Nucl. Fusion* **57** 102019
[20] Griem H R 1997 *Principles of Plasma Spectroscopy* (Cambridge: Cambridge University Press)
[21] Shao C Q, Zhao J Y and Zang Q, Han X F, Xi X Q, Yang J H, Chen H and Hu A L 2014 *Plasma. Sci. Technol.* **16** 721
[22] Shen Y C, Fu J, Lyu Bo *et al.* 2016 *Nucl. Tech.* **39** 020603 (in Chinese)
[23] http://adas.phys.strath.ac.uk
[24] Huang X L, Morita S, Oishi T *et al.* 2017 *Nucl. Fusion* **57** 086031
[25] Chowdhuri M B, Ghosh J, Banerjee S *et al.* 2013 *Nucl. Fusion* **53** 023006
[26] Delgado-Aparicio L, Bitter M, Granetz R, Reinke M and Beiersdorfer P 2012 *Rev. Sci. Instrum.* **83** 10E517
[27] Duan Y M, Hu L Q, Chen K Y, Du W, Zhang L and Team E A S T 2013 *J. Nucl. Mater.* **438** S338